
Debiasing Kernel-Based Generative Models

Tian Qin
Math department
Lehigh University
Bethlehem, PA 18015
tiq218@lehigh.edu

Wei-Min Huang
Math department
Lehigh University
Bethlehem, PA 18015
wh02@lehigh.edu

Abstract

We propose a novel two-stage framework of generative models named Debiasing Kernel-Based Generative Models (DKGM) with the insights from kernel density estimation (KDE) [18, 22] and stochastic approximation [21]. In the first stage of DKGM, we employ KDE to bypass the obstacles in estimating the density of data without losing too much image quality. One characteristic of KDE is oversmoothing, which makes the generated image blurry. Therefore, in the second stage, we formulate the process of reducing the blurriness of images as a statistical debiasing problem and develop a novel iterative algorithm to improve image quality, which is inspired by the stochastic approximation [21]. Extensive experiments illustrate that the image quality of DKGM on CIFAR10 is comparable to state-of-the-art models such as diffusion models [9] and GAN models [17, 5, 13]. The performance of DKGM on CelebA 128×128 and LSUN (Church) 128×128 is also competitive. We conduct extra experiments to exploit how the bandwidth in KDE affects the sample diversity and debiasing effect of DKGM. The connections between DKGM and score-based models [24] are also discussed.

1 Introduction

Generative models have been used to generate high-quality samples in many fields of machine learning. More specifically, Generative adversarial networks (GANs), autoregressive models, and diffusion models have synthesized high-fidelity images and realistic speech and video [8, 1, 9, 3, 12, 16, 30, 10]. Moreover, diffusion models gained popularity in the field of image generation. Most of the generative models share the spirit of sampling new data from pure noise, and the generated data should be consistent with the observed data distribution as much as possible. For example, VAE [14], GAN [8] and diffusion models [9] typically estimate the density of the image distribution $p(\mathbf{x})$ for generation. As a result, VAE suffers from the restricted structure of latent space; GAN falls ill with model collapse due to the subtleness of objective function and diffusion model is slow in generating new images with dedicated backward process. On the other hand, modern generative models always involve two structures. For instance, VAE requires encoder and decoder; GAN needs generator and discriminator and diffusion models has forward and backward processes.

In this paper, we will propose a novel two-stage (asymmetric structure) model to bypass the obstacles in estimating the density of data without losing too much image quality. More specifically, the main contributions of our work can be summarized as followings:

1. We first formulate the generation task as a problem of kernel density estimation, which is the first stage of our model.
2. As to the second stage, we propose a novel debiasing algorithm to enhance the quality of KDE sampled image. The idea is inspired by the stochastic approximation proposed in [21]. The entire two-stage model is named Debiasing Kernel Based Generative Model (DKGM).

3. The implementation of DKGM involves two networks, one is used to generate initial new images by kernel density sampling, the other is to improve the image quality. The experiments demonstrate that DKGM is comparable to many baseline methods in the sense of FID and inception score. The ablation studies also show that the stage 2 of DKGM improves the sample quality (sharpness)[29] in general.

The remaining sections of this paper are organized as following schema. In section 2, we provided some preliminaries about KDE, stochastic approximation and theoretical results. Based on analysis in section 2, we introduced the two-stage model DKGM in section 3. The comparisons between DKGM and other modern generative models in benchmark datasets are illustrated in section 4. In addition, we constructed a numerical example to show the effect of the proposed debiasing algorithm in section 4.1. Section 5 discusses limitations of DKGM and suggests some future directions.

2 Preliminary

2.1 Kernel density estimation (KDE)

For simplicity, we only consider the one-dimension case. Given X_1, \dots, X_m be i.i.d random variables with a continuous density function f , [18] and [22] proposed kernel density estimate $p_m(x)$ for estimating $p(x)$ at a fixed point $x \in \mathbb{R}$,

$$p_m(x) = \frac{1}{mb_m} \sum_{k=1}^m K\left(\frac{x - X_k}{b_m}\right) \quad (1)$$

where K is an appropriate kernel function such that $\int K(x)dx = 1$ and the positive number b_m is called bandwidth such that $b_m \rightarrow 0, mb_m \rightarrow \infty$ as $m \rightarrow \infty$. By convention, literature about VAE [14], GAN [8] and Diffusion models [9] typically estimates data distribution $p(\mathbf{x})$ for generation. However the generation with KDE is straightforward as we can essentially generate new data without deriving or estimating the data density. More specifically, if we let the kernel be Gaussian distribution, sampling from the corresponding kernel density estimate $p_m(x)$ involves two steps:

1. Randomly pick one data point x_i from the data $\{x_1, x_2, \dots, x_n\}$ included in the KDE
2. Given point x_i , draw a value from the Gaussian $N(x_i, b_m^2)$ centered at x_i and of standard deviation b_m (the bandwidth)

Approximating the true density function p with $p_m(x)$, we have the following inequality of empirical likelihood $\log(x)$:

$$\begin{aligned} \log p(x) \approx \log p_m(x) &= \log \left[\frac{1}{mb_m} \sum_{k=1}^m K\left(\frac{x - X_k}{b_m}\right) \right] \\ &\geq \sum_{k=1}^m \log \left[\frac{1}{mb_m} K\left(\frac{x - X_k}{b_m}\right) \right] \end{aligned} \quad (2)$$

For a given datapoint x and kernel function K , the smaller the distance between x and KDE generated sample X_k is, the larger the RHS of the inequality (2) will be. To this sense, if we can model the a network generating the KDE samples around the original input x , the empirical likelihood $\log p(x)$ will be improved. Inequality (2) inspires us to develop the kernel based generation model in section 3.1. Next, we will introduce the concept of the bias of data restoration to enhance the quality of KDE samples.

2.2 Bias of data restoration

Let \mathbf{x}^1 be the original data and $\hat{\mathbf{x}}$ is the restored data from certain networks. If we view $\hat{\mathbf{x}}$ as an estimator of true data point, it is natural to define the bias of restored data $\hat{\mathbf{x}}$ as following:

$$\text{Bias}(\hat{\mathbf{x}}) = \mathbf{x} - \mathbb{E}[\hat{\mathbf{x}}|\mathbf{x}] \quad (3)$$

¹We will use bold letter \mathbf{x} to denote the high-dimension data point.

where the expectation is taken over all possible restored $\hat{\mathbf{x}}$ given true data is \mathbf{x} .

This is an analogue of the mean bias of an estimator in statistic inference [4]. As one of the most important and mostly used concepts of statistical inference, unbiasedness of an estimator ensures that the target estimator estimates the unknown parameter θ properly in the sense of average.

If the bias term in (3) is negligible, we can say the restored data $\hat{\mathbf{x}}$ is satisfactory. Otherwise, it's natural to subtract the estimated bias from initial restored data to obtain less biased data. However, the exact formula of bias in (3) is unavailable in most cases as the derivation of the expectation is complicated in real world applications. To tackle with this issue, for the initially reconstructed data $\hat{\mathbf{x}}$, we consider the following equation

$$\hat{\mathbf{x}} = \mathbb{E}[\tilde{\mathbf{x}}|\mathbf{x}^*] \quad (4)$$

where $\tilde{\mathbf{x}}$ is the version of restored data given input is \mathbf{x}^* and the conditional expectation is taken over all possible restoration data $\tilde{\mathbf{x}}$ given input data is \mathbf{x}^* . In other words, we want to solve for \mathbf{x}^* which satisfies equation (4) and we claim that the solution \mathbf{x}^* will be approximately unbiased with respect to the true data \mathbf{x} under certain conditions, i.e. $E[\mathbf{x}^*|\mathbf{x}] \approx \mathbf{x}$. Given $\hat{\mathbf{x}}$, we assume that the restoration process is random² and the conditional expectation can be represented by a differentiable bijective map $H : \mathcal{X} \rightarrow \mathcal{X}$. For example, we have $\mathbb{E}[\tilde{\mathbf{x}}|\mathbf{x}] = H(\mathbf{x})$ and $\mathbb{E}[\tilde{\mathbf{x}}|\mathbf{x}^*] = H(\mathbf{x}^*)$. The bijectivity of map H assures the one-to-one corresponding between $\hat{\mathbf{x}}$ and \mathbf{x}^* . That is to say, for each $\hat{\mathbf{x}}$ we can find a unique \mathbf{x}^* and if $\hat{\mathbf{x}}$ is random, \mathbf{x}^* will be random as well. In many real cases, we have $\mathcal{X} = \mathbb{R}^p$. To illustrate the core idea, we assume $p = 1$ in the following derivation.

Given true data \mathbf{x} , take the conditional expectation on both side of (4), and we obtain

$$\mathbb{E}[\hat{\mathbf{x}}|\mathbf{x}] = \mathbb{E}[H(\mathbf{x}^*)|\mathbf{x}] \quad (5)$$

Applying the Taylor expansion of $H(\mathbf{x}^*)$ around $\mathbb{E}[\mathbf{x}^*|\mathbf{x}]$, we have

$$\begin{aligned} H(\mathbf{x}^*) &= H(\mathbb{E}[\mathbf{x}^*|\mathbf{x}]) + H'(\mathbb{E}[\mathbf{x}^*|\mathbf{x}]) \cdot (\mathbf{x}^* - \mathbb{E}[\mathbf{x}^*|\mathbf{x}]) \\ &\quad + \frac{1}{2}H''(\mathbb{E}[\mathbf{x}^*|\mathbf{x}]) \cdot (\mathbf{x}^* - \mathbb{E}[\mathbf{x}^*|\mathbf{x}])^2 \\ &\quad + O(|\mathbf{x}^* - \mathbb{E}[\mathbf{x}^*|\mathbf{x}]|^3) \end{aligned} \quad (6)$$

If H is nearly linear, i.e. $H'' \approx 0$, plugging identity (6) into equation (5) gives us the following approximation

$$H(\mathbf{x}) \approx H(\mathbb{E}[\mathbf{x}^*|\mathbf{x}])$$

The bijectivity of H implies that the solution \mathbf{x}^* of (4) is approximately unbiased, i.e. $\mathbb{E}[\mathbf{x}^*|\mathbf{x}] \approx \mathbf{x}$. It can be viewed as a debiased version of initial restoration $\hat{\mathbf{x}}$. The analysis above can be generalized to vector-valued function H and works for the cases when $p > 1$. Consequently, the bias reduction boils down to solving the inverse problem in (4), which can be approached by the stochastic approximation method invented by [21].

2.3 Stochastic approximation

In one dimensional case, [21] proposed to solve the equation $M(x) = \alpha$ where $M(x) = \int_{-\infty}^{\infty} y dF(y|x)$ by a stochastic sequence generated by following iteration:

$$x_{k+1} - x_k = a_k(\alpha - y_k) \quad (7)$$

where y_k is a realization of the random variable which has the distribution of $F(y|x_k)$.

Under certain regularity conditions, [21] shown that if sequence a_k satisfies $\sum a_k = \infty$, and $\sum a_k^2 < \infty$ then the iterated sequence of $\{x_k\}$ will converges to the root θ , which satisfies the original equation $M(\theta) = \alpha$, in L^2 (also in probability). [2] proved a stronger sense of convergence that the sequence $\{x_k\}$ generated by (7) actually converges to the root θ with probability one (almost surely) under weaker conditions.

Similarly, in order to solve equation (4) of data restoration, we consider the following iteration for multivariate case of \mathbf{x} , whose dimension is p :

$$\hat{\mathbf{x}}_{k+1} - \hat{\mathbf{x}}_k = a_k(\hat{\mathbf{x}}_0 - \tilde{\mathbf{x}}_k), \quad k \geq 0 \quad (8)$$

²This assumption only aims to facilitate the theoretical derivation. In practice, the restoration stage (second stage) of DKGM doesn't have to be random as we model the conditional expectation by networks directly.

where the scalar weight coefficient a_k is appropriately selected. $\hat{\mathbf{x}}_0$ is the initial data and $\tilde{\mathbf{x}}_k$ is the restored data given input is $\hat{\mathbf{x}}_k$, i.e. $\tilde{\mathbf{x}}_k$ follows the distribution $F(\tilde{\mathbf{x}}|\hat{\mathbf{x}}_k)$. Denote the i -th coordinate of function H as H_i and $\hat{\mathbf{x}}_0$ as $\alpha = (\alpha_1, \dots, \alpha_p)$ for the clean notations and consider the following set of assumptions **A1** – **A5**:

- (A1): $\sum_{k=1}^{\infty} a_k = \infty, \sum_{k=1}^{\infty} a_k^2 < \infty$.
- (A2): For each dimension $i \in \{1, 2, \dots, p\}$: $H_i(\mathbf{x}) < \alpha_i$ for $x_i < \mathbf{x}_i^*$ and $H_i(\mathbf{x}) > \alpha_i$ for $x_i > \mathbf{x}_i^*$ and $H_i(\mathbf{x}^*) = \alpha_i$, where $\mathbf{x} = (x_1, \dots, x_p) \in \mathbb{R}^d$ and $\mathbf{x}^* = (x_1^*, \dots, x_p^*) \in \mathbb{R}^d$
- (A3): For every $\delta > 0$ and dimension $i \in \{1, 2, \dots, p\}$, function $H_i(\mathbf{x})$ is strictly increasing for each coordinate j w.r.t \mathbf{x} , if $|x_j - \mathbf{x}_j^*| < \delta$ where $\mathbf{x} = (x_1, \dots, x_p) \in \mathbb{R}^d$ and $\mathbf{x}^* = (x_1^*, \dots, x_p^*) \in \mathbb{R}^d$
- (A4): For every $\epsilon > 0$ and coordinate $i \in \{1, 2, \dots, p\}$

$$\inf_{\|\mathbf{x} - \mathbf{x}^*\| > \epsilon} \|H_i(\mathbf{x}) - \alpha_i\| > 0$$

where $\|\cdot\|$ is L_2 norm in our setting.

- (A5): $e_k = E [E [\|\tilde{\mathbf{x}}_k - \alpha\|^2 | \hat{\mathbf{x}}_k]] \leq h^2 < \infty$ for each integer $k \geq 0$,

Theorem 2.1 gives a convergence result of iteration process in (8) based on assumptions **A1** – **A5**. The proof is a multivariate version of the argument given by [21]. See Appendix A.1

Theorem 2.1. *Under assumptions A1 – A5, the sequence of vector $\{\hat{\mathbf{x}}_k\}$ generated by iteration (8) converges to \mathbf{x}^* in probability, which is the solution of the inverse problem $\hat{\mathbf{x}}_0 = H(\mathbf{x}^*)$.*

Assumptions **A2** – **A4** control the local performance of the map H , which implicitly require the decent quality of base model. Indeed, in the experiments, we found that a standard U-Net structure is able to generate good quality of debiased images. The uniform boundedness of the difference between iterated restored data and ideal debiased data in assumption **A5** can be satisfied as long as the restoration process is stable.

In section 2.2, we see that the solution of (5) is unbiased once the reconstruction map H is linear. In addition, the contracting structure of U-Net can be used to approximate the identity map between original data and debiased data. As a consequence, the learned restoration process is expected to be close to a linear map. This observation makes the idea of iterative debiasing promising.

The choice of weight coefficients a_k in assumption **A1** is flexible. In next section, we will illustrate the connection of weight coefficients with the SDE version of iteration process (7).

2.4 SDE version of iteration process (7) and a choice of weight coefficients a_k

According to [21], at k -th iteration, we can reconstruct $\tilde{\mathbf{x}}_k$ for m times and replace $\tilde{\mathbf{x}}_k$ in (8) with the arithmetic mean of m reconstructions, which is denoted as $\bar{\tilde{\mathbf{x}}}_{k,m}$, i.e. the iteration (7) becomes:

$$\hat{\mathbf{x}}_{k+1} - \hat{\mathbf{x}}_k = a_k(\hat{\mathbf{x}}_0 - \bar{\tilde{\mathbf{x}}}_{k,m}), \quad k \geq 0 \quad (9)$$

where $\bar{\tilde{\mathbf{x}}}_{k,m} = \frac{\tilde{\mathbf{x}}_{k1} + \dots + \tilde{\mathbf{x}}_{km}}{m}$ and $\tilde{\mathbf{x}}_{ki}$, ($i = 1, 2, \dots, m$) are reconstructed data given input data is $\hat{\mathbf{x}}_k$. If we write $a_k = \eta u_k$, where η is fixed step size and u_k is adjustable learning rate, iteration (9) can be reformulated as follows:

$$\begin{aligned} \hat{\mathbf{x}}_{k+1} &= \hat{\mathbf{x}}_k + \eta u_k(\hat{\mathbf{x}}_0 - \bar{\tilde{\mathbf{x}}}_{k,m}) \\ &= \hat{\mathbf{x}}_k + \eta u_k(\hat{\mathbf{x}}_0 - E_{\tilde{\mathbf{x}}_k}[\tilde{\mathbf{x}}] + E_{\tilde{\mathbf{x}}_k}[\tilde{\mathbf{x}}] - \bar{\tilde{\mathbf{x}}}_{k,m}) \\ &= \hat{\mathbf{x}}_k + \eta u_k(\hat{\mathbf{x}}_0 - f(\hat{\mathbf{x}}_k)) + \eta u_k(f(\hat{\mathbf{x}}_k) - \bar{\tilde{\mathbf{x}}}_{k,m}) \end{aligned} \quad (10)$$

[15] gives a weak approximation SDE of (10):

$$d\mathbf{x}_t = -u_t(f(\mathbf{x}_t) - \mathbf{x}_0)dt + u_t\sqrt{\eta\Sigma(\mathbf{x}_t)}dW_t, \mathbf{x}_0 = \hat{\mathbf{x}}_0 \quad (11)$$

where $f(x) = E_{\tilde{\mathbf{x}}}[\tilde{\mathbf{x}}], \Sigma(\mathbf{x}) = \frac{1}{m}Var_{\tilde{\mathbf{x}}}(\tilde{\mathbf{x}})$ and W_t is the white noise process. $u_t \in [0, 1]$ is the continuous time analogue of the adjustment factor u_k with the usual identification $t = k\eta$ and m represents the number of reconstruction times. It's now natural to consider optimizing weight coefficients through the adjustable learning rate u_t under the constraint (11).

[15] considered a simpler case which assumes that the variance function $\Sigma(\mathbf{x}) = \Sigma$ which is constant all the time. If we further assume the linearity of f , i.e. $f(\mathbf{x}_t) = a\mathbf{x}_t$, proposition 2.2 gives us a version of optimal adjustment of learning rate u_t . The proof can be found in [15].

Proposition 2.2 ([15]). *Denote $m_t = \frac{1}{2}\mathbb{E}[(\mathbf{x}_t - \mathbf{x}_0)^2]$ as the cost function of u_t . We assume that the variance function $\Sigma(\mathbf{x}) = \Sigma > 0$ and $f(\mathbf{x}) = a\mathbf{x}$, $a \in \mathbb{R}$. Consider the following optimal control problem for learning rate u_t with fixed stopping time T :*

$$\begin{aligned} \min_{u: [0, T] \rightarrow [0, 1]} \quad & m_T \\ \text{s.t.} \quad & d\mathbf{x}_t = -u_t(a\mathbf{x}_t - \mathbf{x}_0)dt + u_t\sqrt{\eta\Sigma}dW_t \\ & \mathbf{x}_0 = \hat{\mathbf{x}}_0 \end{aligned} \tag{12}$$

then the optimal control policy would be

$$u_t^* = \begin{cases} 1 & a \leq 0 \quad \text{or} \quad t \leq t^* \\ \frac{1}{1+a(t-t^*)} & a > 0 \quad \text{or} \quad t > t^* \end{cases} \tag{13}$$

where $t^* = \frac{1}{2a} \log\left(\frac{4m_0}{\eta\Sigma} - 1\right)$.

Few observations based on proposition 2.2:

1. The optimal adjustment policy implies that the maximum learning rate should be used in initial phase where the drift term is dominant. In the fluctuation phase, the noise term dominates the process so the optimal policy will use the $\sim 1/t$ annealing schedule to reduce the effect of the fluctuation.
2. More surprisingly, we can verify such adjustment policy satisfy the sufficient condition **A1** of the convergence of Stochastic approximation in Theorem 2.1 and [21]. (L_1 divergent and L_2 convergent).

Note that it's unrealistic to find the phase change point t^* in practice as it requires the knowledge of coefficient a in $f(\mathbf{x})$ and the constant variance Σ . However, the $\sim 1/t$ annealing schedule provides us a candidate of weight coefficient a_k . For simplicity and stability, we set $a_k = \frac{1}{k}$, which is the harmonic series and satisfies the assumption **A1** introduced in section 2.3. Our experiments in section 4 also indicate that setting $a_k = \frac{1}{k}$ is good enough in practice.

2.5 Choice of network to approximate restored data $\tilde{\mathbf{x}}$ given input $\hat{\mathbf{x}}_k$

Vanilla denoising autoencoder (DAE) is a natural choice as it keeps the same input and output size. However, the vanilla DAE has difficulty in recovering original images with simple model structure such as CNN, which is likely to violate the linearity assumption in bias reduction. Another choice is U-Net [9]. Its contracting path (encoder) can fuse the local information with the global feature through skip connections. In that sense, we conjecture that U-Net is better suitable to the assumptions in section 2.3. We then propose the corresponding debiasing structure in section 3.

3 Debiasing Kernel Based Generative Models

In this part, we propose a novel two-stage generative model named Debiasing Kernel Based Generative Model (DKGM) based on the idea of KDE and stochastic approximation introduced in section 2. In section 3.1, we introduce the first stage of DKGM aiming to build a kernel based generative model, which can be trained as the same in denoising model. Since the initial image generated is blurry (See Fig. 4(a)) due to the noise added into the input, we then develop a novel iterative debiasing method in section 3.2 to enhance the quality of initial generation, which is the second stage of DKGM. The main difference between DKGM and diffusion models is that DKGM directly reduces the bias of initial generated images while diffusion models requires artificial noises added in the original data.

3.1 First stage: Initial generation model

The objective function in first stage is straightforward. To maximize the lower bound of empirical log-likelihood function in 2, we need to maximize the log of KDE for each data point $\mathbf{x}^{(i)}$. For

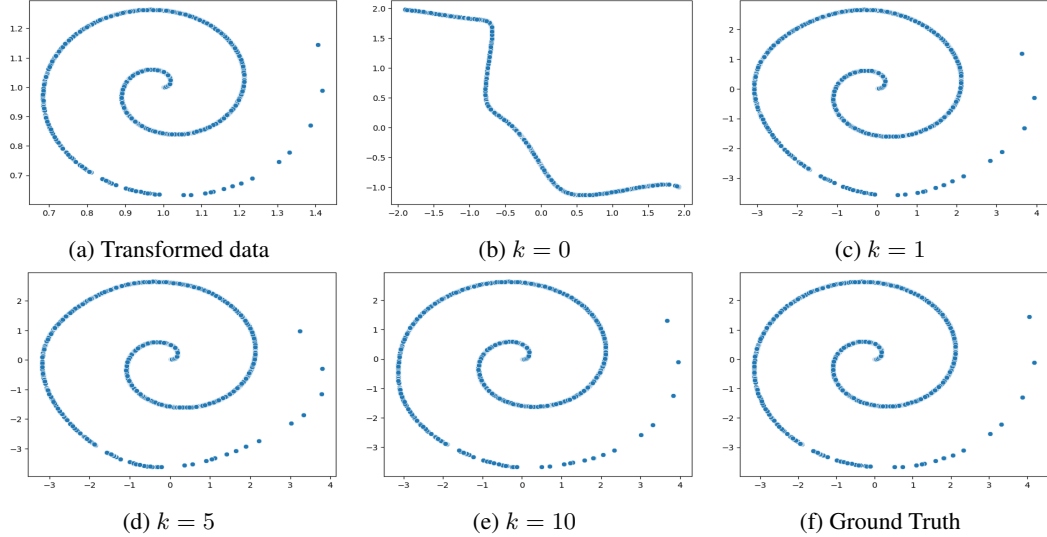


Figure 1: The Stage 2 DKGM trained on 1-d swiss roll data. The leftmost subplot (a) is the transformed data, which is the input of stage 2 model. Subplot (f) represents the ground truth. The rest subplots (b)-(d) are reconstructed data corresponding to different values of $k > 0$.

simplicity, we chose gaussian density to be the kernel function in KDE and the target function is reduced to

$$\sum_{k=1}^m \|\mathbf{x}^{(i)} - \hat{\mathbf{x}}_k^{(i)}\|^2 = \sum_{k=1}^m \|\mathbf{x}^{(i)} - f_{\theta}(\mathbf{x}^{(i)} + \epsilon_k^{(i)})\|^2 \quad (14)$$

where the map f_{θ} is modeled by a neural network and the noise ϵ_k follows a certain distribution with bandwidth \mathbf{h} . The geometric interpretation of the target function (14) is, we want the trained model f_{θ} to sample the data in the neighborhood of the original input, which is exactly the intuition of KDE. As we can expect, the quality of sampled data simply through f_{θ} won't be good enough due to the over smoothness from KDE. For instance, Figure 4(a) shows that the generated images from stage one are somehow blurry. Therefore, we introduce a debiasing method in second stage to enhance the quality of generated data in stage 1. In our experiments, we found that a large number of KDE samples m per datapoint will lead to out of memory issues in training and we can actually set m to be 1 as long as model f_{θ} is strong enough, e.g. U-Net.

3.2 Second stage: Iterative debiasing

Figure 4(a) displays the KDE sampled images from stage 1 of DKGM, which are somehow blurry. This phenomenon can be explained by the gaussian noise introduced in each datapoint. By one-dimension Taylor expansion, the function f_{θ} in (14) can be expanded as $f_{\theta}(x^{(i)} + \epsilon) \approx f_{\theta}(x^{(i)}) + f'_{\theta}(x^{(i)}) \cdot \epsilon$. Then the blurriness comes from the convolution between $f_{\theta}(x^{(i)})$ and $f'_{\theta}(x^{(i)}) \cdot \epsilon$, where the second term is equivalent to a gaussian kernel. To reduce the blurriness from the KDE sampling, we introduce the second stage of DKGM with the iteration equation in (8).

In the second stage, we should train another model to reduce the blurriness from first stage. Empirically, we found that it's better to train the debiasing model on Gaussian blurred data rather than the direct KDE samples from the first stage. For Gaussian-blurred data, we meant to perform Gaussian blurring on the image by Gaussian kernel with kernel size (bandwidth) b , which is realized by adding a convolution layer in the model. Among our experiments, we found that setting b uniformly distributed during the training epochs will benefit the performance of entire model. The building block of second stage model is still U-Net. Except for the initial Gaussian blurred data, we iteratively used the output of U-Net to approximate the t -th bias term $\hat{\mathbf{x}}_0 - \tilde{\mathbf{x}}_t$ in iteration (8). See the flow chart in Figure 2. There are two strategies of training the iterative restoration described in Figure 2. One is to fully train each U-Net so that we can use it to approximate $\hat{\mathbf{x}}_0 - \tilde{\mathbf{x}}_k$. However, this strategy requires us to train the U-Nets sequentially which can be time consuming for large number of iteration steps k . The other

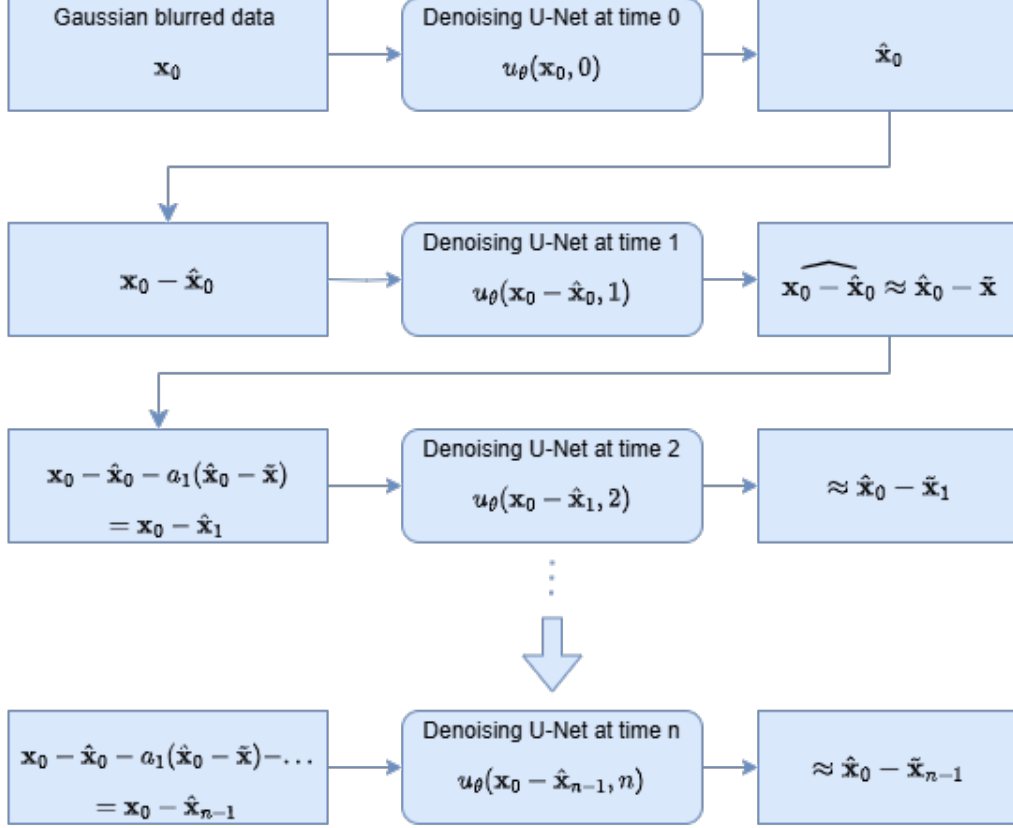


Figure 2: The flow chart of second stage DKGM

strategy is similar to the implementation in [9], which trains a time-step embedded U-Net with a single target function. This method is time efficient but has a high demand for memory. In this paper, we decided to employ the second strategy for the sake of time efficiency. Algorithm 1 summarizes the forward implementation of the second stage of DKGM using the time-step embedded U-Net $u_\gamma(\cdot, t)$

Algorithm 1 Second stage of DKGM

Require: Gaussian Blurred data $\bar{\mathbf{x}}_g$ with bandwidth b . Iteration times n . Weight coefficients

$$a_j = \frac{1}{j}, j = 1, \dots, n.$$

1: **Initialization:**

2: Set $\mathbf{x}_0 = \bar{\mathbf{x}}_g$ and evaluate $\hat{\mathbf{x}}_0 = u_\gamma(\mathbf{x}_0, 0)$

3: **for** $t \in \{1, \dots, n\}$ **do**

4: $\hat{\mathbf{x}}_t = \hat{\mathbf{x}}_{t-1} + a_t \cdot u_\gamma(\hat{\mathbf{x}}_0 - \hat{\mathbf{x}}_{t-1}, t)$ where we use $u_\gamma(\hat{\mathbf{x}}_0 - \hat{\mathbf{x}}_{t-1}, t)$ to approximate $\mathbf{x}_0 - \tilde{\mathbf{x}}_{t-1}$

5: **Return:** $\hat{\mathbf{x}}_n$

Given the output from Algorithm 1, we employed the following comprehensive target function to train the time-step embedded U-Nets simultaneously at i -th gaussian-blurred data point $\bar{\mathbf{x}}_g^{(i)}$:

$$\tilde{\mathcal{L}}(\theta; \hat{\mathbf{x}}^{(i)}) = \|\bar{\mathbf{x}}_g^{(i)} - \hat{\mathbf{x}}_n^{(i)}\|^2 \quad (15)$$

where

$$\begin{aligned} \hat{\mathbf{x}}_n^{(i)} &= \hat{\mathbf{x}}_0^{(i)} + \sum_{t=1}^n \frac{1}{t} \cdot u_\gamma(\hat{\mathbf{x}}_0^{(i)} - \hat{\mathbf{x}}_{t-1}^{(i)}, t), \\ \hat{\mathbf{x}}_0^{(i)} &= u_\gamma(\mathbf{x}_0^{(i)}, 0) = u_\gamma(\bar{\mathbf{x}}_g^{(i)}, 0) \end{aligned} \quad (16)$$



Figure 3: LSUN Church samples from DKGM ($\alpha = 0.5, b \sim \text{Unif}[0.5, 1.0]$), FID=4.99

The subscript γ represents learnable parameters in time-step embedded U-Net $u_\gamma(\cdot, t)$. With f_θ and $u_\gamma(\cdot, t)$ trained, we can use the output of stage 1 KDE sampling as the input of trained stage 2. The detailed procedure is summarized in Algorithm 2.

Algorithm 2 Sampling with noise level α

Require: $\epsilon \sim N(\mathbf{0}, I), \mathbf{x} \sim p_{data}, f_\theta, u_\gamma(\cdot, t), \alpha.$

1: **Stage 1: KDE sampling**

2: $\hat{\mathbf{x}}_{kde} = f_\theta(\mathbf{x} + \alpha\epsilon)$

3: **Stage 2: Iterative debiasing**

4: $\hat{\mathbf{x}}_0 = u_\gamma(\hat{\mathbf{x}}_{kde}, 0)$

5: **for** $t \in \{1, \dots, n\}$ **do**

6: $\hat{\mathbf{x}}_t = \hat{\mathbf{x}}_{t-1} + a_t \cdot u_\gamma(\hat{\mathbf{x}}_{kde} - \hat{\mathbf{x}}_{t-1}, t)$ where we use $u_\gamma(\hat{\mathbf{x}}_{kde} - \hat{\mathbf{x}}_{t-1}, t)$ to approximate $\hat{\mathbf{x}}_{kde} - \tilde{\mathbf{x}}_{t-1}$

7: **Return:** $\hat{\mathbf{x}}_n$

4 Experiments

In this section, a toy example will be provided to demonstrate the effect of debiasing steps proposed in section 3.2. We can see increasing the number of bias iterations indeed benefits the restoration. After that, we compare the sample quality of DKGM with other state-of-art algorithms in few real datasets. The inception scores and FID scores are reported in Table 1. Inception.v3 [28] is employed as default model in both measurements, which is a standard practice in literature. All model architectures and training details are provided in Appendix C and D.

4.1 Toy example: 1-d Swiss Roll

[11] designs a 1-d swiss roll manifold which is essentially a one dimensional spiral function and vanilla VAEs failed to capture the underlying manifold and density. Additionally, a one dimensional swiss roll distribution can also be successfully learned by a diffusion model, as illustrated in [23]. Section 2.3 implies that stage 2 of DKGM is similar to the diffusion process. Observing how the reconstruction of stage 2 of DKGM evolves with the debiasing steps k in this toy example could give us more insights into the debiasing-type model. For simplicity, the base model of DKGM in this example is vanilla autoencoder. Detailed experiment settings are available in Appendix C.

Figure 1 demonstrates that increasing the number of bias iterations in DKGM indeed benefits the reconstructed data. The poor result in vanilla autoencoder reconstruction ($k = 0$) is consistent

Table 1: Baseline results on Unconditional CIFAR10 datasets.

Model	IS(std)	FID
DDPM(L_{simple}) [9]	9.46(0.11)	3.17
EBM [6]	6.78(-)	38.2
NCSN [25]	8.87(0.12)	25.32
SNGAN [17]	8.22(0.02)	21.7
SNGAN-DDLS [5]	9.09(0.1)	15.42
StyleGAN2 + ADA (v1) [13]	9.74(0.05)	3.26
DKGM ($\alpha = 0.5, b \sim Unif[0.5, 1]$)	8.62(0.18)	6.42

with the results in [11] as the latent space learned by the initial vanilla autoencoder is deficient in complicated data manifold and density. The reconstructed manifold from transformed data is closer to the ground truth as k increases. More interestingly, unlike carefully designed transformation functions in normalizing flow models [20], the debiasing part of DKGM shows the potential of learning density on non-euclidean manifolds.

Theoretically, setting large k is always beneficial to the debiased reconstruction, as implied by Theorem 2.1. While in practice, larger k could lead to heavier computation cost and overfitting. How to choose optimal k relies on the complexity of base models and the data. We leave this as the future research.

4.2 Real datasets

Table 1 reports Inception scores(IS), FID scores on CIFAR10. We can see our DKGM model achieves comparable Inception scores and FID scores to many models, including the DDPM. The FID score is based on the training set, which is standard practice[9]. We also achieved 4.99 FID score in LSUN (Church) 128×128 and 11.87 FID score in CelebA 128×128 . See Fig 3 for generated sample quality and Appendix F for more information. The detailed information for training parameters are attached in Appendix D.

4.2.1 Enhancement from Stage 2 of DKGM

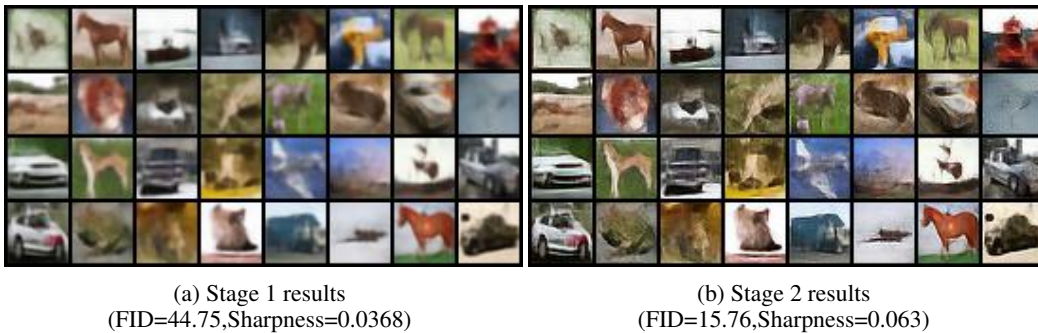


Figure 4: Randomly generated samples on unconditional CIFAR10 through two stages in DKGM (a) Generated samples from the model trained in Stage 1 with noise level $\alpha = 1.0$ (b) Enhanced samples after stage 2 of DKGM with $b \sim Unif(0.8, 1.2)$

Figure 4 provides the generated images on unconditional CIFAR10 using DKGM. Comparing the samples in Figure 4(a) and Figure 4(b), we can see that the debiasing model in stage 2 of DKGM empirically improves the quality and sharpness of samples generated in stage 1, as verified by FID scores and sharpness.

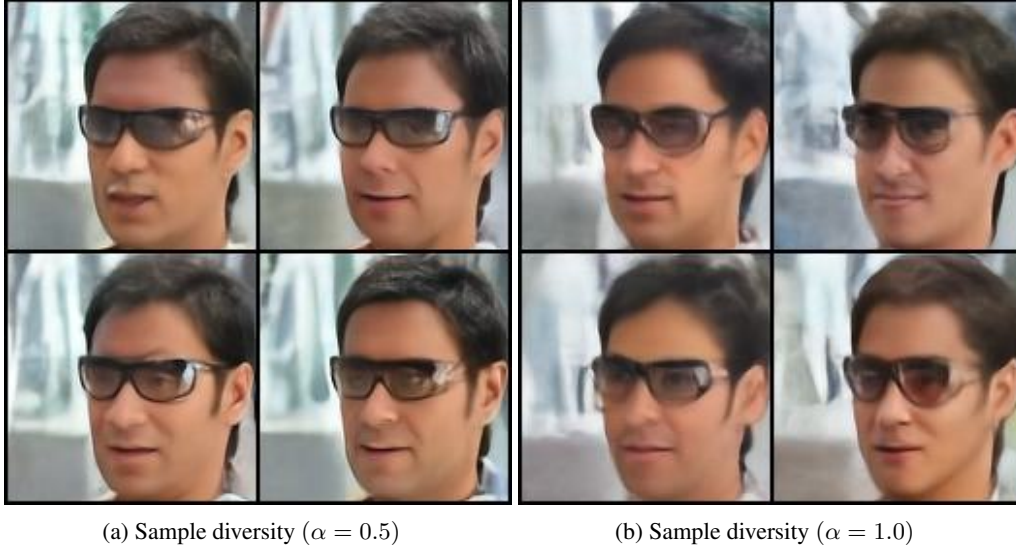


Figure 5: Randomly generated samples on CelebA 128×128 with same input under different noise levels of DKGM. (a) Generated samples from DKGM trained with noise level $\alpha = 0.5$ (b) Generated samples from DKGM trained with noise level $\alpha = 1.0$

4.2.2 Noise level α in DKGM

To see the effect of noise level in stage 1, we provide KDE samples on CelebA 128×128 with same input under different noise levels. When the noise level is low, we see that samples share high-level attribute while when the noise level is high, the samples are more diversified (e.g. hair cut styles are clearly different for samples in Figure 5(b) , which is anticipated according to the idea of KDE.

4.2.3 Effect of gaussian blurring kernel bandwidth b

In this section, we performed extra experiments to see how the choice of Gaussian blurring kernel bandwidth would affect the FID, Inception score and sharpness of DKGM on CIFRA10 dataset. The results displayed in Table 2 reveal that tuning bandwidth b can be beneficial and the uniformly distributed bandwidth b with the appropriate range performs better in practice.

Table 2: Effect of gaussian blurring kernel bandwidth on CIFRA10 ($\alpha = 0.5$)

BANDWIDTH b	FID	IS(STD)	SHARPNESS
$b = 0.8$	26.55	8.99(0.09)	0.1406
$b = 0.6$	7.65	8.72(0.13)	0.0642
$b = 0.5$	7.94	8.27(0.10)	0.0492
$b \sim Unif(0.8, 1.2)^*$	19.4	9.1(0.15)	0.085
$b \sim Unif(0.5, 1.0)$	6.42	8.62(0.18)	0.056

*The symbol " \sim " means that the bandwidth in gaussian blurring layer is uniformly distributed during the training.

4.2.4 Ablation studies of Stage 1 model

We have theoretically and empirically verified the debiasing efficacy of second stage DKGM. Since the trainings of two stages in DKGM are separated, it's natural to ask would the debiasing algorithm still work if we replace the stage 1 model with other generative models which also incorporate Gaussian noises? Table 3 illustrates the change of sample quality of DKGM with different Stage 1(S1) models on CIFAR10 and the results indicate that stage 2 of DKGM performs best when connected with KDE and it indeed benefits the sample quality more or less, except for the FID of DDPM. One possible reason is that the backward diffusion process focuses more on distributional characteristics and less on details. However, stage 2 of DKGM improved sharpness in general, indicating it is able to fill in the "gaps" in terms of sharpness. The stage 2 DKGM trained with

$b \sim \text{Unif}[0.5, 1]$ is used for all S1 models listed in Table 3. FID and Sharpness are evaluated on testing set. The S1 model implementations all follow the standard practice. (See more details in Appendix E)

Table 3: Change of sample quality of DKGM with different S1 models on Unconditional CIFAR10

S1 model	$\Delta\text{FID}(\%)*$	$\Delta\text{Sharpness}(\%)$
VAE	-9%	4%
DCGAN	-10%	45%
DDPM	24%	55%
Ours KDE model ($\alpha = 0.5$)	-64%	36%

* $\Delta\text{FID}(\%)$ is the increase/decrease percentage of FID for DKGM with new S1 models with respect to S1 models. Similar definition for $\Delta\text{Sharpness}(\%)$

5 Limitation and discussion

5.1 Limitations of DKGM

Time efficiency of training stage 2 of DKGM

As we mentioned in section 3.2, the current implementation of stage 2 DKGM training can be time consuming if we needs more iteration steps k in debiasing step³. One possible reason is the choice of base model in the iteration. Our experiments indicate that U-Net is indeed a good choice while the time efficiency of deliberate network would be the sacrifice. How to design a more efficient network structure (e.g. CNN) is one of our future works.

Trade off between sample quality and sample diversity

In sections 4.2.2 and 4.2.3, we have seen that the noise level in stage 1 of DKGM controls the sample diversity and the bandwidth in stage 2 affects the sample quality. Table 2 implies that there might be an optimal bandwidth given each noise level. How to incorporate noise level and blurring bandwidth is an interesting open question. On the other hand, it’s possible to embed these two parameters into the training of DKGM and we will leave it as future research.

5.2 Connection between score-based models

Recall the SDE (11) in section 2.4, a stochastic version of iterative debiasing in stage 2 of DKGM:

$$d\mathbf{x}_t = -u_t(f(\mathbf{x}_t) - \mathbf{x}_0)dt + u_t\sqrt{\eta\Sigma(\mathbf{x}_t)}dW_t, \quad \mathbf{x}_0 = \hat{\mathbf{x}}_0$$

where $f(\mathbf{x}_t) = E[\tilde{\mathbf{x}}_t|\mathbf{x}_0]$, $\Sigma(\mathbf{x}) = \frac{1}{m} \text{Var}_{\tilde{\mathbf{x}}}(\tilde{\mathbf{x}})$, W_t is the white noise process and \mathbf{x}_0 is the initial data. With Tweedie’s formula [7], we have $E[\tilde{\mathbf{x}}_t|\mathbf{x}_0] \approx \mathbf{x}_0 + \sigma^2\delta \cdot \nabla_{\tilde{\mathbf{x}}_0} \log p_\delta(\mathbf{x}_0)$ if $\mathbf{x}_0 = \tilde{\mathbf{x}}_t + N(0, \sigma^2\delta)$. For simplicity, we assume $u_t = 1$ for $t \in [0, 1]$. Then the SDE above becomes

$$d\mathbf{x}_t = -\nabla_{\tilde{\mathbf{x}}_0} p_\delta(\mathbf{x}_0)dt + \sqrt{\eta\Sigma(\mathbf{x}_t)}dW_t$$

where $p_\delta(\mathbf{x}_0)$ represents the density of \mathbf{x}_0 given parameter δ and the term $\nabla_{\tilde{\mathbf{x}}_0} \log p_\delta(\mathbf{x}_0)$ is typically called score function of distribution $p_\delta(\mathbf{x}_0)$ in literature [24, 26, 27]. To this sense, DKGM is somehow related with score-based models if the posterior expectation term $f(\mathbf{x}_t) = E[\tilde{\mathbf{x}}_t|\mathbf{x}_0]$ has appropriate forms. This observation further demonstrates the flexibility of DKGM as we don’t explicitly assume the functional form of $E[\tilde{\mathbf{x}}_t|\mathbf{x}_0]$ at stage 2 of DKGM.

5.3 Data augmentation

As shown in Figure 6, by DKGM we can generate high-quality similar images in the neighborhood of the input image. One possible downstream application would be the data augmentation in image classification tasks. The generation step in DKGM is essentially a type of KDE sampling, which

³In most of experiments, we set $k = 4$, which is good enough.

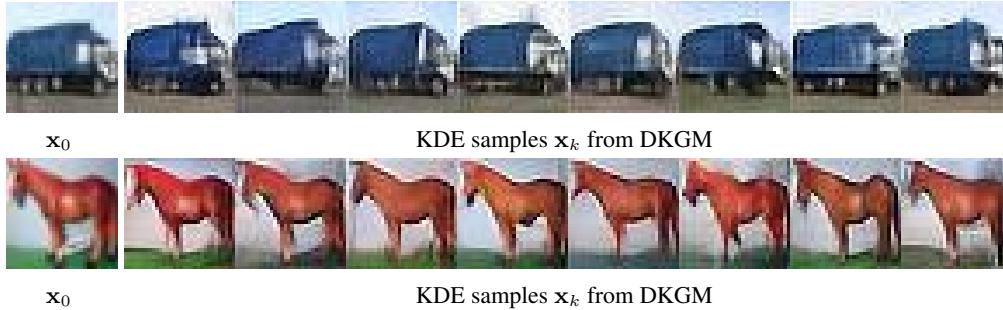


Figure 6: KDE samples on Cifar10 under the same input x_0 with DKGM trained under noise level $\alpha = 0.5$. The leftmost images are the input of DKGM and the rest of images are generated images from DKGM.

generates similar images in the neighborhood of the input image. The edge is that if we can sample more representative images for certain labels, the trained classifier can see more informative examples for underrepresented labels, which is especially useful for imbalanced datasets such as cancer detection. In that way, we can augment the original training set with DKGM to boost the classifier performance.

Impact Statement

This paper aims to propose a novel generative model. The theoretical results should not have negative societal impacts. One possible negative impact resulting from DKGM might be the misuse in producing fake images which may lead to security issues in some face recognition based systems. Few mitigation strategies: (1) gate the release of models for commercial use;(2) add a mechanism for monitoring fake images generated by models such as the discriminator in GAN. All benchmark datasets used in this paper are public and well known to the machine learning community.

References

- [1] Yoshua Bengio, Réjean Ducharme, and Pascal Vincent. A neural probabilistic language model. In T. Leen, T. Dietterich, and V. Tresp, editors, *Advances in Neural Information Processing Systems*, volume 13. MIT Press, 2000.
- [2] Julius R. Blum. Approximation Methods which Converge with Probability one. *The Annals of Mathematical Statistics*, 25(2):382 – 386, 1954.
- [3] Andrew Brock, Jeff Donahue, and Karen Simonyan. Large scale GAN training for high fidelity natural image synthesis. In *International Conference on Learning Representations*, 2019.
- [4] G. Casella and R.L. Berger. *Statistical Inference*. Duxbury advanced series in statistics and decision sciences. Thomson Learning, 2002.
- [5] Tong Che, Ruixiang Zhang, Jascha Sohl-Dickstein, Hugo Larochelle, Liam Paull, Yuan Cao, and Yoshua Bengio. Your gan is secretly an energy-based model and you should use discriminator driven latent sampling. In *Proceedings of the 34th International Conference on Neural Information Processing Systems*, NIPS '20, Red Hook, NY, USA, 2020. Curran Associates Inc.
- [6] Yilun Du and Igor Mordatch. Implicit generation and modeling with energy based models. In H. Wallach, H. Larochelle, A. Beygelzimer, F. d'Alché-Buc, E. Fox, and R. Garnett, editors, *Advances in Neural Information Processing Systems*, volume 32. Curran Associates, Inc., 2019.
- [7] Bradley Efron. Tweedie’s formula and selection bias. *Journal of the American Statistical Association*, 106(496):1602–1614, 2011. PMID: 22505788.
- [8] Ian J. Goodfellow, Jean Pouget-Abadie, Mehdi Mirza, Bing Xu, David Warde-Farley, Sherjil Ozair, Aaron C. Courville, and Yoshua Bengio. Generative adversarial nets. In *Neural Information Processing Systems*, 2014.

- [9] Jonathan Ho, Ajay Jain, and Pieter Abbeel. Denoising diffusion probabilistic models. In H. Larochelle, M. Ranzato, R. Hadsell, M.F. Balcan, and H. Lin, editors, *Advances in Neural Information Processing Systems*, volume 33, pages 6840–6851. Curran Associates, Inc., 2020.
- [10] Jonathan Ho, Tim Salimans, Alexey Gritsenko, William Chan, Mohammad Norouzi, and David J Fleet. Video diffusion models. In S. Koyejo, S. Mohamed, A. Agarwal, D. Belgrave, K. Cho, and A. Oh, editors, *Advances in Neural Information Processing Systems*, volume 35, pages 8633–8646. Curran Associates, Inc., 2022.
- [11] Christian Horvat and Jean-Pascal Pfister. Denoising normalizing flow. In *Neural Information Processing Systems*, 2021.
- [12] Nal Kalchbrenner, Aäron van den Oord, Karen Simonyan, Ivo Danihelka, Oriol Vinyals, Alex Graves, and Koray Kavukcuoglu. Video pixel networks. In Doina Precup and Yee Whye Teh, editors, *Proceedings of the 34th International Conference on Machine Learning*, volume 70 of *Proceedings of Machine Learning Research*, pages 1771–1779. PMLR, 06–11 Aug 2017.
- [13] Tero Karras, Miika Aittala, Janne Hellsten, Samuli Laine, Jaakko Lehtinen, and Timo Aila. Training generative adversarial networks with limited data. In *Proceedings of the 34th International Conference on Neural Information Processing Systems*, NIPS '20, Red Hook, NY, USA, 2020. Curran Associates Inc.
- [14] Diederik P. Kingma and Max Welling. Auto-encoding variational bayes. *CoRR*, abs/1312.6114, 2013.
- [15] Qianxiao Li, Cheng Tai, and Weinan E. Stochastic modified equations and adaptive stochastic gradient algorithms. In Doina Precup and Yee Whye Teh, editors, *Proceedings of the 34th International Conference on Machine Learning*, volume 70 of *Proceedings of Machine Learning Research*, pages 2101–2110. PMLR, 06–11 Aug 2017.
- [16] Jacob Menick and Nal Kalchbrenner. GENERATING HIGH FIDELITY IMAGES WITH SUB-SCALE PIXEL NETWORKS AND MULTIDIMENSIONAL UPSCALING. In *International Conference on Learning Representations*, 2019.
- [17] Takeru Miyato, Toshiki Kataoka, Masanori Koyama, and Yuichi Yoshida. Spectral normalization for generative adversarial networks. In *International Conference on Learning Representations*, 2018.
- [18] Emanuel Parzen. On Estimation of a Probability Density Function and Mode. *The Annals of Mathematical Statistics*, 33(3):1065 – 1076, 1962.
- [19] Alec Radford, Luke Metz, and Soumith Chintala. Unsupervised representation learning with deep convolutional generative adversarial networks. *CoRR*, abs/1511.06434, 2015.
- [20] Danilo Jimenez Rezende and Shakir Mohamed. Variational inference with normalizing flows. *ArXiv*, abs/1505.05770, 2015.
- [21] Herbert Robbins and Sutton Monro. A Stochastic Approximation Method. *The Annals of Mathematical Statistics*, 22(3):400 – 407, 1951.
- [22] Murray Rosenblatt. Remarks on Some Nonparametric Estimates of a Density Function. *The Annals of Mathematical Statistics*, 27(3):832 – 837, 1956.
- [23] Jascha Sohl-Dickstein, Eric Weiss, Niru Maheswaranathan, and Surya Ganguli. Deep unsupervised learning using nonequilibrium thermodynamics. In Francis Bach and David Blei, editors, *Proceedings of the 32nd International Conference on Machine Learning*, volume 37 of *Proceedings of Machine Learning Research*, pages 2256–2265, Lille, France, 07–09 Jul 2015. PMLR.
- [24] Yang Song and Stefano Ermon. *Generative modeling by estimating gradients of the data distribution*. Curran Associates Inc., Red Hook, NY, USA, 2019.
- [25] Yang Song and Stefano Ermon. Generative modeling by estimating gradients of the data distribution. In H. Wallach, H. Larochelle, A. Beygelzimer, F. d'Alché-Buc, E. Fox, and R. Garnett, editors, *Advances in Neural Information Processing Systems*, volume 32. Curran Associates, Inc., 2019.
- [26] Yang Song, Sahaj Garg, Jiaxin Shi, and Stefano Ermon. Sliced score matching: A scalable approach to density and score estimation. In *Conference on Uncertainty in Artificial Intelligence*, 2019.

- [27] Yang Song, Jascha Narain Sohl-Dickstein, Diederik P. Kingma, Abhishek Kumar, Stefano Ermon, and Ben Poole. Score-based generative modeling through stochastic differential equations. *ArXiv*, abs/2011.13456, 2020.
- [28] Christian Szegedy, Vincent Vanhoucke, Sergey Ioffe, Jon Shlens, and Zbigniew Wojna. Rethinking the inception architecture for computer vision. In *2016 IEEE Conference on Computer Vision and Pattern Recognition (CVPR)*, pages 2818–2826, 2016.
- [29] Ilya Tolstikhin, Olivier Bousquet, Sylvain Gelly, and Bernhard Schoelkopf. Wasserstein auto-encoders. In *International Conference on Learning Representations*, 2018.
- [30] Aäron van den Oord, Sander Dieleman, Heiga Zen, Karen Simonyan, Oriol Vinyals, Alexander Graves, Nal Kalchbrenner, Andrew Senior, and Koray Kavukcuoglu. Wavenet: A generative model for raw audio. In *Arxiv*, 2016.

A Proofs

A.1 Proof of Theorem 2.1

Let $b_k = E\|\hat{\mathbf{x}}_k - \mathbf{x}^*\|^2$. We can then express b_{n+1} as following:

$$\begin{aligned}
b_{k+1} &= E\|\hat{\mathbf{x}}_{k+1} - \mathbf{x}^*\|_2^2 = E[E(\|\hat{\mathbf{x}}_{k+1} - \mathbf{x}^*\|_2^2 | \hat{\mathbf{x}}_k)] \\
&= E[E[(\hat{\mathbf{x}}_{k+1} - \mathbf{x}^*)^T (\hat{\mathbf{x}}_{k+1} - \mathbf{x}^*) | \mathbf{x}^*]] \\
&= E[E[(\hat{\mathbf{x}}_k - \mathbf{x}^* + a_k(\alpha - \tilde{\mathbf{x}}_k))^T (\hat{\mathbf{x}}_k - \mathbf{x}^* + a_k(\alpha - \tilde{\mathbf{x}}_k)) | \hat{\mathbf{x}}_k]] \\
&= E[E[(\hat{\mathbf{x}}_k - \mathbf{x}^*)^T (\hat{\mathbf{x}}_k - \mathbf{x}^*) + 2a_k(\hat{\mathbf{x}}_k - \mathbf{x}^*)^T (\alpha - \tilde{\mathbf{x}}_k) + a_k^2(\alpha - \tilde{\mathbf{x}}_k)^T (\alpha - \tilde{\mathbf{x}}_k) | \hat{\mathbf{x}}_k]] \\
&= b_k - 2a_k E[(\hat{\mathbf{x}}_k - \mathbf{x}^*)^T (H(\hat{\mathbf{x}}_k) - \alpha)] + a_k^2 E[E(\|\alpha - \tilde{\mathbf{x}}_k\|_2^2 | \hat{\mathbf{x}}_k)]
\end{aligned} \tag{17}$$

Note that $E[(\hat{\mathbf{x}}_k - \mathbf{x}^*)^T (H(\hat{\mathbf{x}}_k) - \alpha)]$ is a scalar, we can simplify this expression by trace operation:

$$\begin{aligned}
E[(\hat{\mathbf{x}}_k - \mathbf{x}^*)^T (H(\hat{\mathbf{x}}_k) - \alpha)] &= E[\text{tr}\{(\hat{\mathbf{x}}_k - \mathbf{x}^*)^T (H(\hat{\mathbf{x}}_k) - \alpha)\}] \\
&= E[\text{tr}\{(H(\hat{\mathbf{x}}_k) - \alpha)(\hat{\mathbf{x}}_k - \mathbf{x}^*)^T\}] \\
&= \text{tr}\{E[(H(\hat{\mathbf{x}}_k) - \alpha)(\hat{\mathbf{x}}_k - \mathbf{x}^*)^T]\} \\
&= \text{tr}\{B_k\}
\end{aligned}$$

where $B_k = E[(H(\hat{\mathbf{x}}_k) - \alpha)(\hat{\mathbf{x}}_k - \mathbf{x}^*)^T]$ and the third equation comes from the linearity of expectation and trace operation.

Now the equation (17) becomes:

$$b_{k+1} = b_k - 2a_k \text{tr}\{B_k\} + a_k^2 E[E(\|\alpha - \tilde{\mathbf{x}}_k\|_2^2 | \hat{\mathbf{x}}_k)] \tag{18}$$

Summing up first $k + 1$ equations, we obtain:

$$b_{k+1} = b_1 - 2 \sum_{i=0}^k a_i \text{tr}\{B_i\} + \sum_{i=0}^k a_i^2 E[E(\|\alpha - \tilde{\mathbf{x}}_i\|_2^2 | \hat{\mathbf{x}}_i)]$$

Since $b_{k+1} \geq 0$ by definition, we have

$$\begin{aligned}
\sum_{i=0}^k a_i \text{tr}\{B_i\} &\leq \frac{1}{2} \left(b_0 + \sum_{i=0}^k a_i^2 E[E(\|\alpha - \tilde{\mathbf{x}}_i\|_2^2 | \hat{\mathbf{x}}_i)] \right) \\
&\leq \frac{1}{2} \left(b_0 + \sum_{i=0}^k a_i^2 h^2 \right) \quad (\text{Assumption A5})
\end{aligned} \tag{19}$$

By Assumption A1, we can conclude that

$$\sum_{i=1}^{\infty} a_i \text{tr}\{B_i\} \leq \frac{1}{2} \left(b_1 + \sum_{i=1}^{\infty} a_i^2 h^2 \right) < \infty \tag{20}$$

So $\sum_{i=1}^{\infty} a_i \text{tr}\{B_i\}$ exists and

$$\lim_{k \rightarrow \infty} a_k \text{tr}\{B_k\} = 0$$

We claim that the sequence $\hat{\mathbf{x}}_k$ converges to \mathbf{x}^* in probability. Otherwise, there exists an subsequence $\{k_j, j = 1, 2, \dots\}$ of sequence $\{k\}$ and positive number ϵ, η such that

$$P\{\|\hat{\mathbf{x}}_{k_j} - \mathbf{x}^*\| > \eta\} > \epsilon$$

for all k_j . On the other hand, for all k_j we have

$$\begin{aligned}
tr(B_{k_j}) &= tr\{E[(H(\hat{\mathbf{x}}_{k_j}) - \alpha)(\hat{\mathbf{x}}_{k_j} - \mathbf{x}^*)^T]\} \\
&= E[tr\{(H(\hat{\mathbf{x}}_{k_j}) - \alpha)(\hat{\mathbf{x}}_{k_j} - \mathbf{x}^*)^T\}] \\
&= E[(\hat{\mathbf{x}}_{k_j} - \mathbf{x}^*)^T(H(\hat{\mathbf{x}}_{k_j}) - \alpha)] \\
&= E\left[\sum_{i=1}^p (\hat{\mathbf{x}}_{i,k_j} - \mathbf{x}_i^*)(H_i(\hat{\mathbf{x}}_{k_j}) - \alpha_i)\right] \\
&= E\left[\sum_{i=1}^p |\hat{\mathbf{x}}_{i,k_j} - \mathbf{x}_i^*| |H_i(\hat{\mathbf{x}}_{k_j}) - \alpha_i|\right] \\
&\geq \epsilon\eta \inf_{\|\mathbf{x} - \mathbf{x}^*\| > \epsilon} \|H_i(\mathbf{x}) - \alpha_i\| > 0
\end{aligned}$$

for some $i \in \{1, 2, \dots, p\}$. The last three lines come from **A2** – **A4**

It follows that

$$tr(B_{k_j}) > 0$$

for all k_j , which contradicts the inequality (20). We then proves the claim.

B Toy example: 1-d Swiss Roll

Similar to the construction in 4.1, we consider a similar 1 dimensional manifold embedded in \mathbb{R}^2 , a thin spiral. Suppose the latent variable u follows an exponential distribution with rate 1, i.e. the density is $f(u) = e^{-u}$, and we generate the spiral through function

$$g(u) = \frac{\alpha\sqrt{u}}{3}(\cos(\alpha\sqrt{u}), \sin(\alpha\sqrt{u}))^T, \quad \alpha = \frac{4\pi}{3}$$

See ground truth plot in Figure 1(f) . To validate the reconstruction performance of stage 2 DKGM, we perform a simple linear transformation of the ground truth, i.e the transformed spiral has form of

$$\tilde{g}(u) = 0.1g(u) + 1$$

whose plot is illustrated in Figure 1(a) for transformed data.

C Model architecture

C.1 1-d Swiss Roll

Since this is a simple dataset, We employed simple auto-encoders as base models in DKGM. The encoder structure involves two layer of linear mapping composed with tanh sigmoid function . In the last fully connect layer, we set the latent dimensions $d_z = 1$

Encoder:

$$\begin{aligned}
x \in \mathbb{R}^2 &\rightarrow \text{Linear layer } W^{2 \times 4} \rightarrow \text{Tanh} \\
&\rightarrow \text{Linear layer } W^{4 \times 8} \rightarrow \text{Tanh} \\
&\rightarrow \text{Fully connected } (8 \times d_z) \text{ for each parameters}
\end{aligned}$$

Decoder:

$$\begin{aligned}
z \in \mathbb{R}^{d_z} &\rightarrow \text{Fully connected } (d_z \times 4) \rightarrow \text{Tanh} \\
&\rightarrow \text{Linear layer } W^{4 \times 8} \rightarrow \text{Tanh} \\
&\rightarrow \text{Linear layer } W^{8 \times 2} \rightarrow \mathbb{R}^2
\end{aligned}$$

C.2 CIFAR-10

The U-Net implementation for CIFAR-10 follows the work in [9]. More specifically, for the time embedding, all parameters are shared across time, which is specified to the network using the Transformer sinusoidal position embedding [9]. Self-attentions are employed at the 16×16 feature map resolution.

C.3 CelebA 128×128 and LSUN (Church) 128×128

For CelebA 128×128 and LSUN (Church) 128×128 , the U-Net is adjusted to the input size of 128×128 and the self-attentions blocks are removed to reduce the model size.

D Datasets and Training details

We list details for each benchmark dataset in following table

Datasets	# Training samples	# Hold-out samples	Original image size
CIFAR-10	50000	10000	32*32
CelebA 128×128	162770	19867	178*218
LSUN (Church) 128×128	126227	-	256*256

Note that for CIFAR-10, we used default splittings of training sets and testing sets provided in Pytorch (torchvision.datasets). For CelebA 128×128 , we used default validation set as hold-out samples. As to LSUN (Church), the FID score is evaluated on the whole training set for the sake of comparison.

For the training details, we used same training parameters for all algorithms and datasets, as described in following table

DKGM iteration times k	4
Optimizer	Adam with learning rate $3e-4$
Batch size	100 (20 for CelebA and LSUN)
Epochs	50 (20 for CelebA and LSUN)

Our CIFAR10 model has 35.7 million parameters, and our LSUN and CelebA models have 114 million parameters. We used NVIDIA 4070 GPU (8G) for all experiments. Under the training settings in Table above, the training of whole stage of DKGM for CIFAR10 requires 8 hours (2.5 hours for Stage 1 while 5.5 hours for Stage 2) and the training time for CelebA 128×128 and LSUN (Church) 128×128 is nearly 22 hours. (5 hours for Stage 1 training and 17 hours for Stage 2 training).

Calculation of Sharpness

We follow the way in [29] in calculating the sharpness of an image. For each generated image, we first transformed it into grayscale and convolved it with the Laplace filter $\begin{pmatrix} 0 & 1 & 0 \\ 1 & -4 & 1 \\ 0 & 1 & 0 \end{pmatrix}$, computed the variance of the resulting activations and took the average of all variances. The resulting number is denoted as sharpness (larger is better). The blurrier image will have less edges. As a result, the variance of activations will be small as most activations will be close to zero. Note that we averaged the sharpness of all reconstructed images from hold-out samples for each dataset.

E Ablation studies

The implementation of VAE follows a standard encoder-decoder structure. We used fully convolutional architectures with 4×4 convolutional filters for both encoder and decoder in VAE. In encoder, we employed a layer of Adaptive Average pool filter.

Encoder q_ϕ :

$x \in \mathbb{R}^{32 \times 32} \rightarrow 32 \text{ Conv, Stride 2} \rightarrow \text{BatchNorm} \rightarrow \text{ReLU}$
 $\rightarrow 64 \text{ Conv, Stride 2} \rightarrow \text{BatchNorm} \rightarrow \text{ReLU}$
 $\rightarrow 128 \text{ Conv, Stride 2} \rightarrow \text{BatchNorm} \rightarrow \text{ReLU}$
 $\rightarrow 256 \text{ Conv, Stride 2} \rightarrow \text{BatchNorm} \rightarrow \text{ReLU}$
 $\rightarrow \text{AdaptiveAvgPool2d}$
 $\rightarrow \text{Fully connected } (1 * 1 * 256 \times d_z) \text{ for each parameters}$

Decoder p_θ :

$z \in \mathbb{R}^{d_z \times d_z} \rightarrow \text{Fully connected } (d_z \times 1 * 1 * 256)$
 $\rightarrow 128 \text{ ConvTran, Stride 1} \rightarrow \text{BatchNorm} \rightarrow \text{ReLU}$
 $\rightarrow 64 \text{ ConvTran, Stride 2} \rightarrow \text{BatchNorm} \rightarrow \text{ReLU}$
 $\rightarrow 32 \text{ ConvTran, Stride 2} \rightarrow \text{BatchNorm} \rightarrow \text{ReLU}$
 $\rightarrow 3 \text{ ConvTran, Stride 2} \rightarrow \text{Sigmoid}$

The implementation of DCGAN[19] follows the popular structure proposed in [19]. And we still employed 4×4 convolutional filters.

Generator $G(z)$:

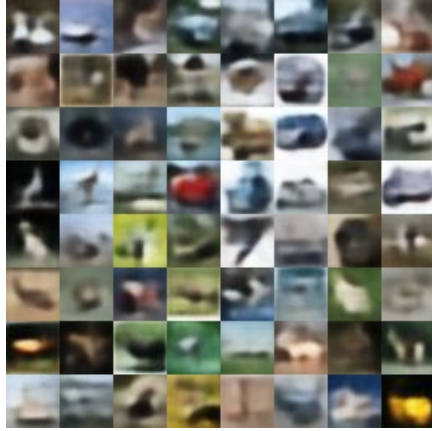
$z \in \mathbb{R}^{100} \rightarrow 512 \text{ ConvTran, Stride 1} \rightarrow \text{BatchNorm} \rightarrow \text{ReLU}$
 $\rightarrow 256 \text{ ConvTran, Stride 2} \rightarrow \text{BatchNorm} \rightarrow \text{ReLU}$
 $\rightarrow 128 \text{ ConvTran, Stride 2} \rightarrow \text{BatchNorm} \rightarrow \text{ReLU}$
 $\rightarrow 3 \text{ ConvTran, Stride 2} \rightarrow \text{Tanh}$

Discriminator $D(x)$:

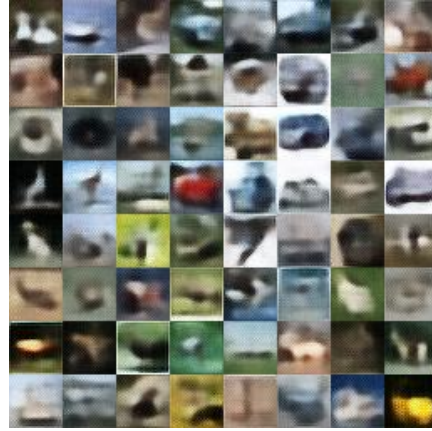
$x \in \mathbb{R}^{32 \times 32} \rightarrow 64 \text{ Conv, Stride 2} \rightarrow \text{BatchNorm} \rightarrow \text{ReLU}$
 $\rightarrow 128 \text{ Conv, Stride 2} \rightarrow \text{BatchNorm} \rightarrow \text{ReLU}$
 $\rightarrow 256 \text{ Conv, Stride 2} \rightarrow \text{BatchNorm} \rightarrow \text{ReLU}$
 $\rightarrow 1 \text{ Conv, Stride 1} \rightarrow \text{Sigmoid}$

The implementation of DDPM follows the structures in [9]. All those S1 models are trained with Batch size 32, Adam learning rate 3e-4 and 50 Epochs.

Using VAE as stage 1 model



Sample from VAE
(FID=120.9, Sharpness=0.0364)



Bias reduced sample with Stage 2 DKGM with $b \sim \text{Unif}(0.5, 1.0)$ (FID=109.8, Sharpness=0.0379)

Figure 7

Using DCGAN as stage 1 model



Generated sample DCGAN (FID=15.42, Sharpness=0.0422)



Bias reduced sample with Stage 2 DKGM with $b \sim \text{Unif}[0.5, 1.0]$ (FID=13.89, Sharpness=0.0585)

Figure 8

Using DDPM as stage 1 model



Generated sample DDPM
(FID=26.45, Sharpness=0.0433)



Bias reduced sample with Stage 2 DKGM with $b \sim$
 $Unif[0.5, 1.0]$ (FID=35.06, Sharpness=0.0669)

Figure 9

F More generated images from DKGM

F.1 Unconditional CIFAR10



Generated sample from Stage 1 DKGM with $\alpha = 1$ (FID=44.75, Sharpness=0.0368) Bias reduced sample with Stage 2 DKGM with $b \sim \text{Unif}[0.8, 1.2]$ (FID=15.76, Sharpness=0.063)

Figure 10

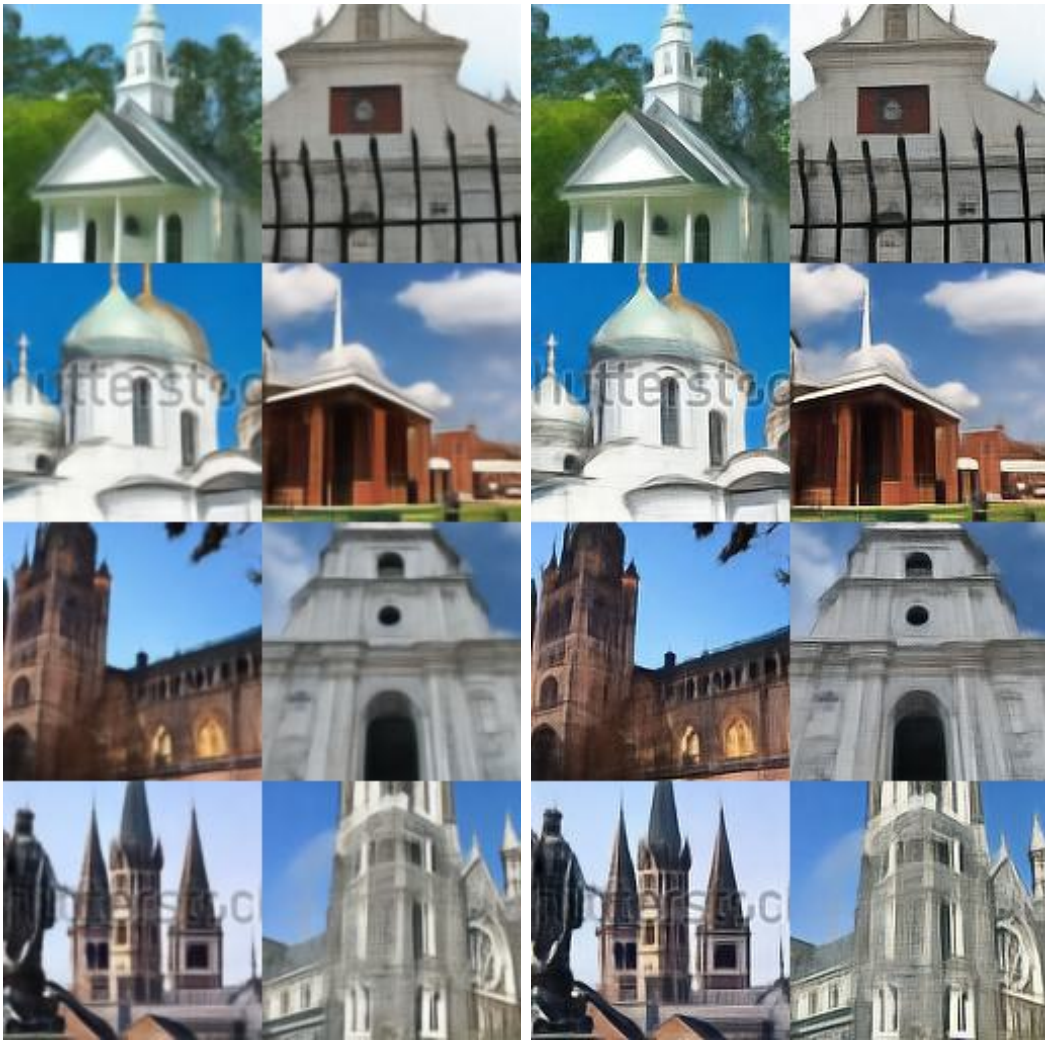
F.2 CelebA 128 × 128



Generated sample from Stage 1 DKGM with $\alpha = 0.5$ (FID=15.57, Sharpness=0.0121) Bias reduced sample with Stage 2 DKGM with $b \sim \text{Unif}[0.5, 1.0]$ (FID=11.87, Sharpness=0.0155)

Figure 11

F3 LSUN Church 128×128



Generated sample from Stage 1 DKGM with $\alpha = 1$ (Bias reduced sample with Stage 2 DKGM with $b \sim \text{Unif}(0.8, 1.2)$) (FID=22.10, Sharpness=0.0127) (FID=13.93, Sharpness=0.0312)

Figure 12



Generated sample from Stage 1 DKGM with $\alpha = \text{Bias reduced sample}$ with Stage 2 DKGM with $b \sim \text{Unif}[0.5, 1.0]$ (FID=7.77, Sharpness=0.0151) (FID=4.99, Sharpness=0.0262)

Figure 13

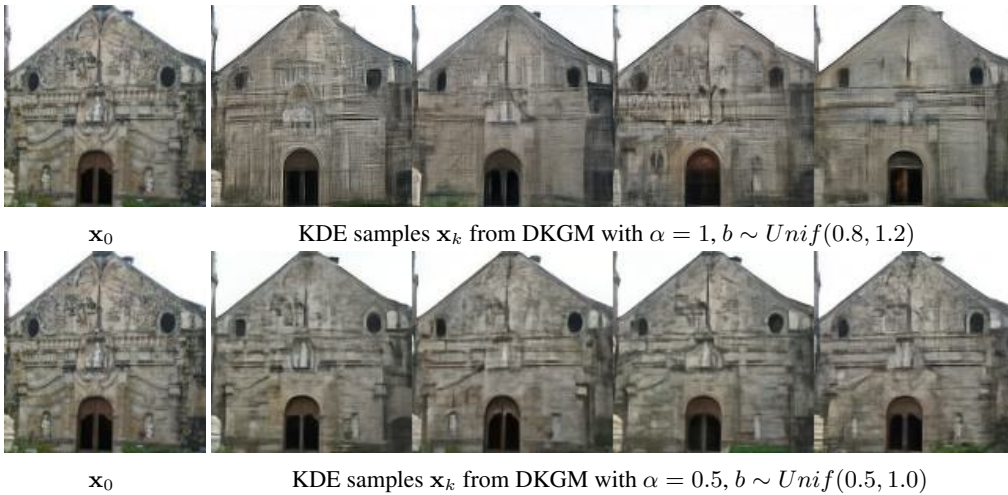


Figure 14: KDE samples on LSUN Church under the same input \mathbf{x}_0 with DKGM trained under different noise levels. The leftmost images are the input of DKGM and the rest of images are generated images from DKGM.